Supporting information

Regulating local chemical softness of collector to homogenize Li deposition for anode-free Li-metal batteries

Jiaming Zhu[1], Cong Kang[1], Xiangjun Xiao[1], Ya Mao[2], Ying Luo[2], Yuheng Wang[3], Quansheng Zhang[3], Yulin Ma[1], Chunyu Du[1], Shuaifeng Lou[1], Fanpeng Kong[1,4,*], Jingying Xie[2,*], Geping Yin[1,*]

1. State Key Laboratory of Space Power-Sources, School of Chemistry and Chemical Engineering, Harbin Institute of Technology, Harbin 150001, China.

2. Shanghai Institute of Space Power-Sources, Shanghai 200245, China.

3. School of Chemical and Environmental Engineering, Shanghai Institute of Technology, Shanghai 201418, China.

4. Chongqing Research Institute of HIT, Chongqing 401135, China.

*Corresponding author: E−mail: yingeping@hit.edu.cn (G, Yin), fpkong@hit.edu.cn (F. Kong), jyxie@mail.sim.ac.cn (J, Xie)

Equation

$$\varphi(E) = -4.44 + W_f \quad (1)$$

$$t_{Li^+} = \frac{I_{SS}(\Delta V - I_0 R_0)}{I_0(\Delta V - I_{SS} R_{SS})} \quad (2)$$

Table

Table S1. Energy barrier during lithium atom diffusion process.

matrices	formation energy barrier	fracture energy barrier
Co/NC	0.38	0.61
Fe/NC	0.42	0.64

matrices	formation energy barrier	fracture energy barrier
Co/NC	0.40	0.63
Cr/NC	0.41	0.62
V/NC	0.53	0.64

Table S2. Adsorption energy between carbon atom and lithium atom

matrices	slab+Li	slab	ΔE
Co/NC	-448.62	-446.70	-1.62
Cr/NC	-450.82	-449.17	-1.35
Fe/NC	-449.33	-447.81	-1.22
Mn/NC	-450.34	-448.92	-1.12
V/NC	-449.74	-448.08	-1.36
NC	-438.21	-437.41	-0.50

Table S3. Nucleation overpotential (η_n) and growth overpotential (η_g) on different matrices

matrices	η_n	η_g	$\Delta\eta$
Co-SAs	25.70	8.30	17.40
FeSAs	26.00	10.50	15.50
VSAs	28.20	15.50	12.70
NiSAs	30.00	9.90	20.10
CrSAs	30.00	15.50	14.50
MnSAs	32.80	19.20	13.60
NC	26.00	14.20	11.80
Cu	48.90	9.60	39.30

Table S4. Energy densities of different cell

cathode	anode	N/P	ecific energy ($Wh\,kg^{-1}$)	vol. energy density ($Wh\,L^{-1}$)
LFP	Gr	1.1	212	501.4
LFP	Li	1	276.7	661.6
LFP	Li	0	280.7	707.6
NCM	Gr	1.1	361	954.4
NCM	Li	1	537.8	1545.8
NCM	Li	0	550.8	1772.4

Figures

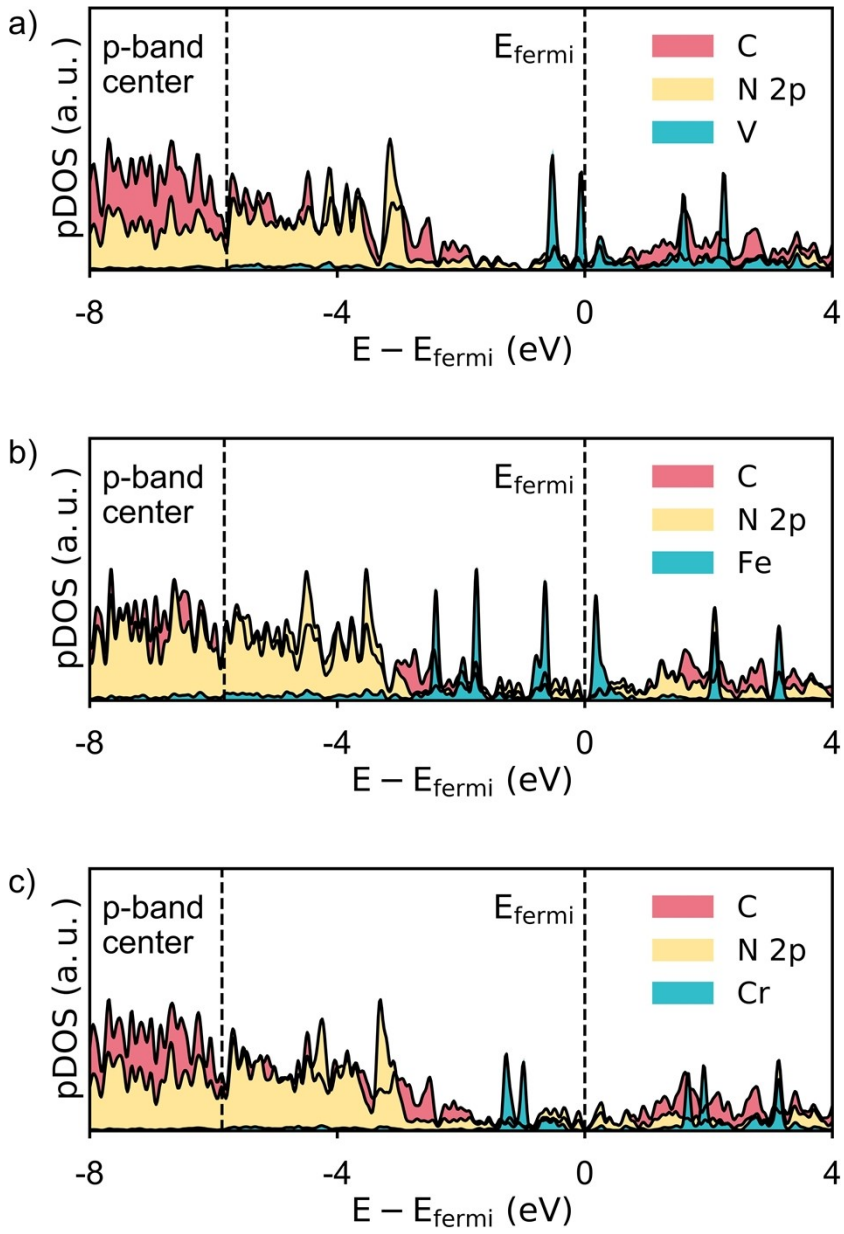

Figure S1. Projected DOS (PDOS) for C, N 2p orbitals and V/Fe/Cr 3d orbitals including V/NC , Fe/NC and Cr/NC.

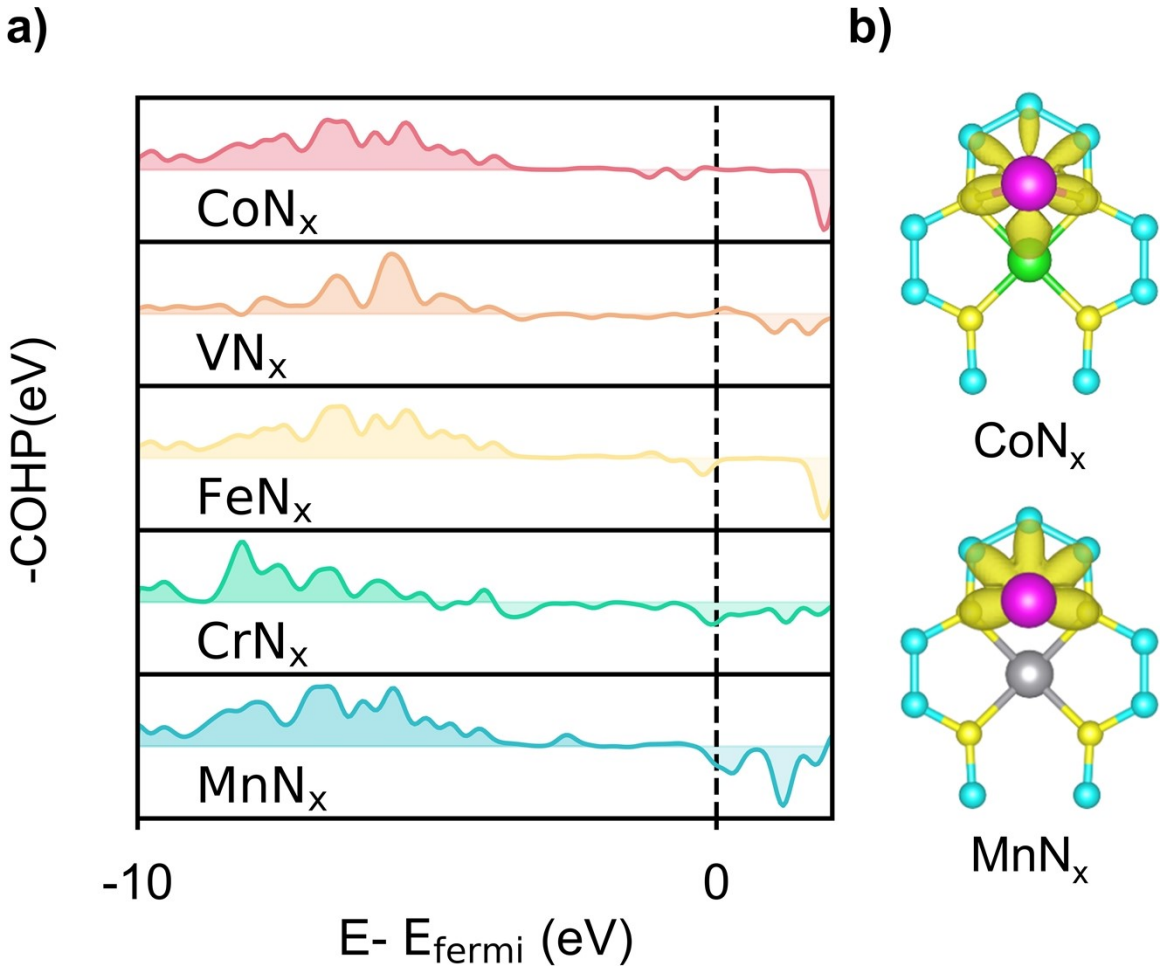

Figure S2. (a) Crystal orbital Hamilton population (-COHP) of Li adsorbed on different matrices. The area above the horizontal axis represents bonding states. (b) Hirshfeld surface of Li adsorbed on the Co/NC and Co/NC.

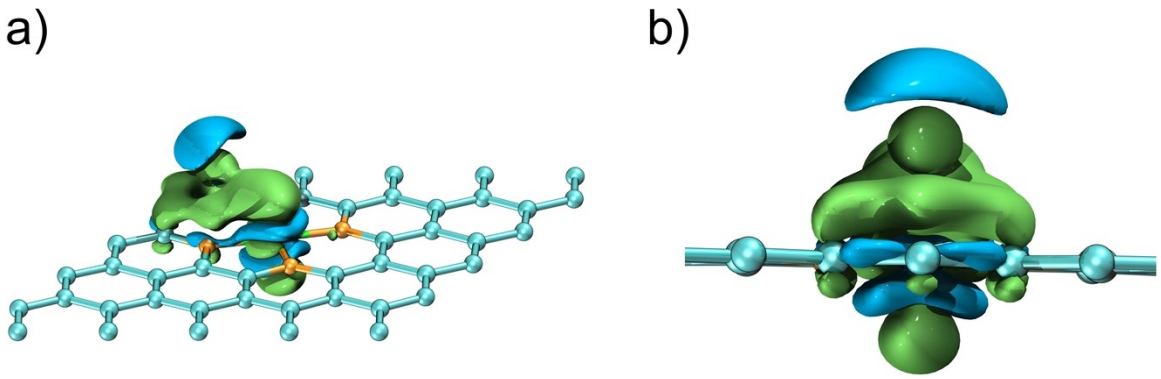

Figure S3. Differential charge density map of Li ion adsorption on Co/NC.

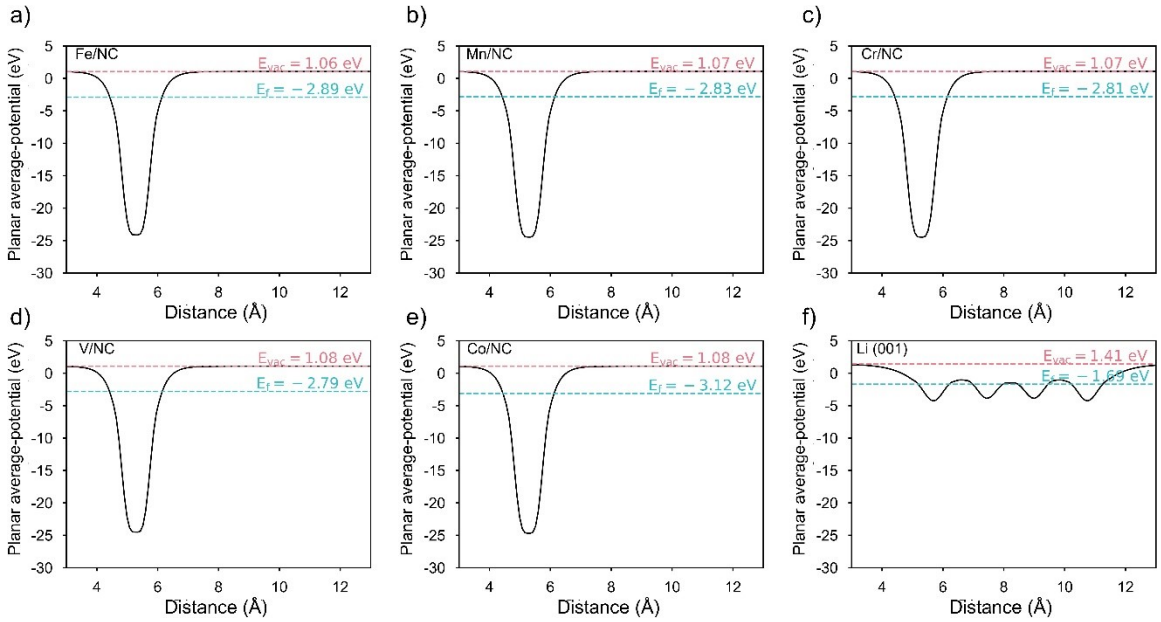

Figure S4. Surface work function (SWF) of different matrices.

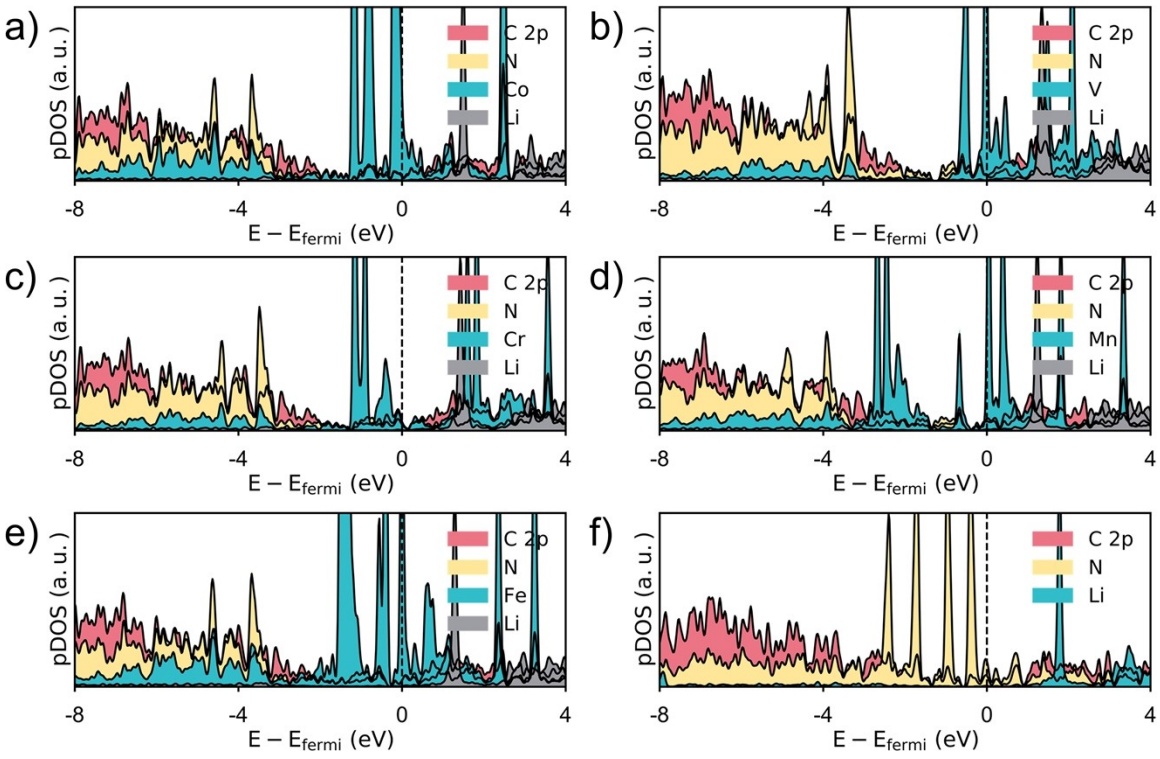

Figure S5. PDOS including (a) Co/NC, (b) V/NC, (c) Cr/NC, (d) Mn/NC, (e) Fe/NC, (f) NC.

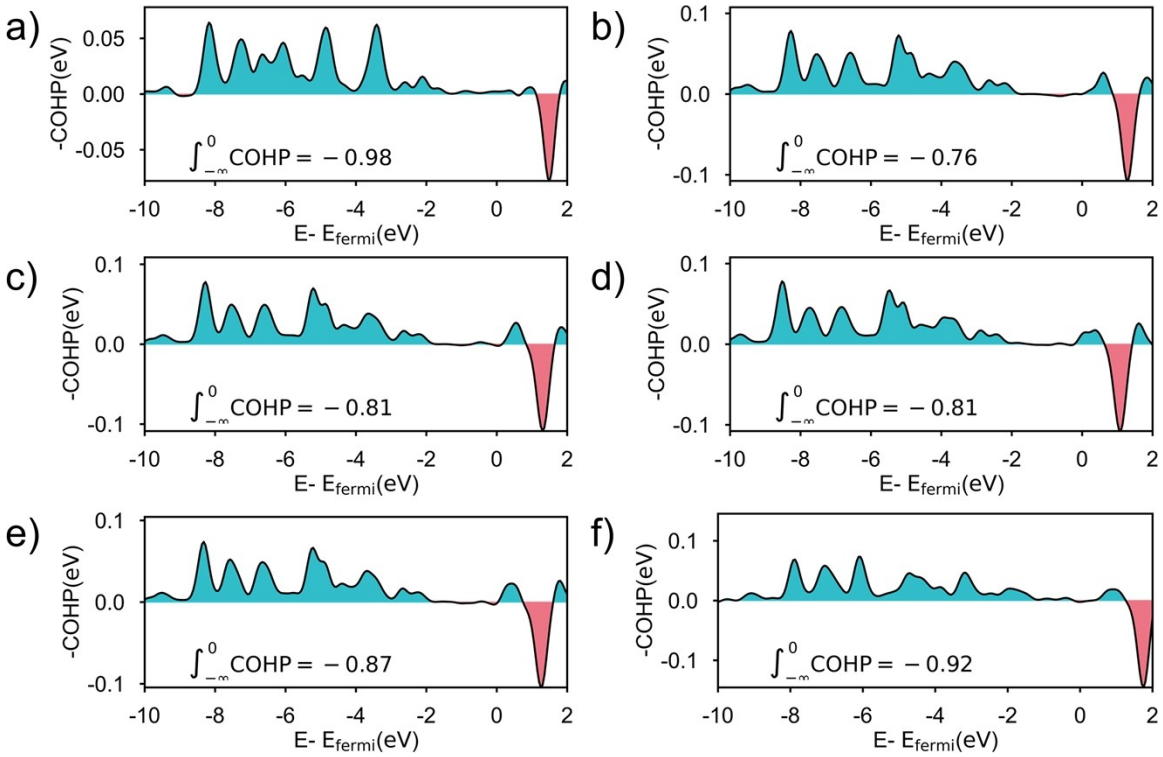

Figure S6. -COHP between C and Li atom including (a) Co/NC, (b) V/NC, (c) Cr/NC, (d) Mn/NC, (e) Fe/NC, (f) NC. The area above the horizontal axis represents bonding states.

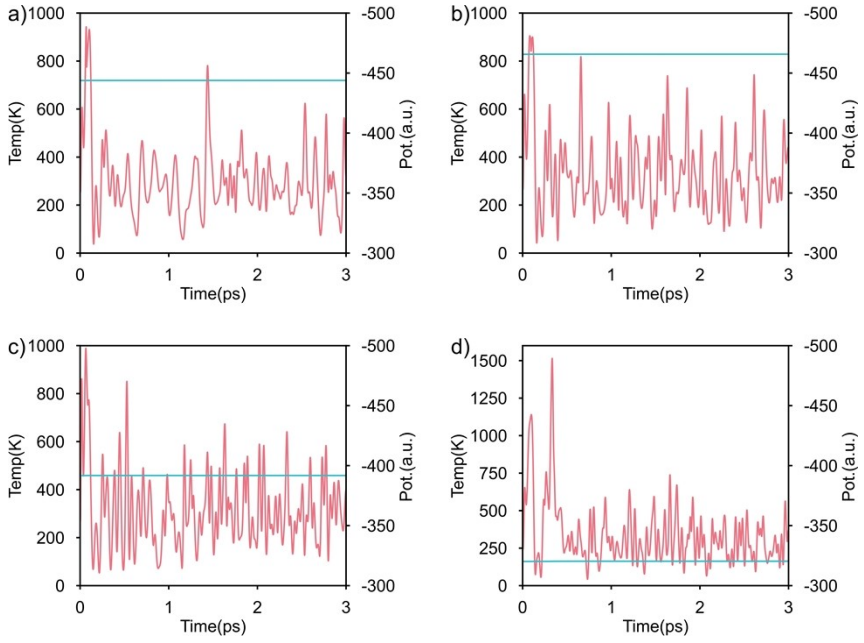

Figure S7. Variation of temperature and energy with time step for AIMD simulations on (a) Fe/NC, (b) Co/NC, (c) V/NC and (d) NC.

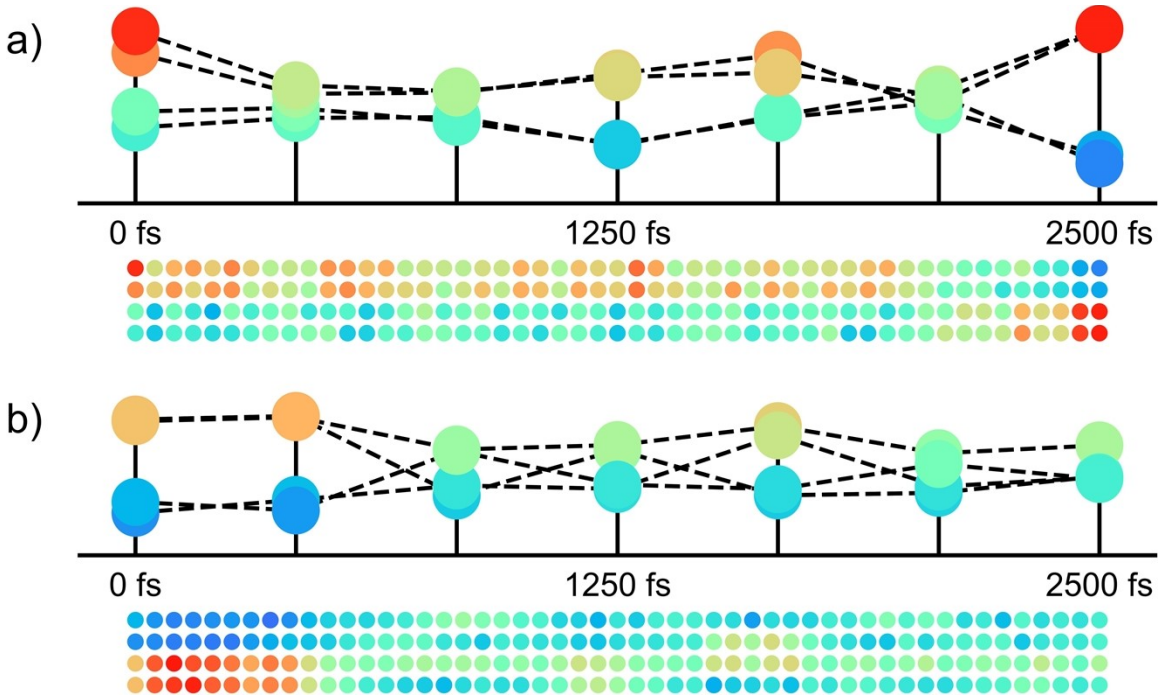

Figure S8. AIMD calculations of the lithium structure in relation to the temporal evolution of the Li-Li bond length on (a) V/NC, and (b) Fe/NC.

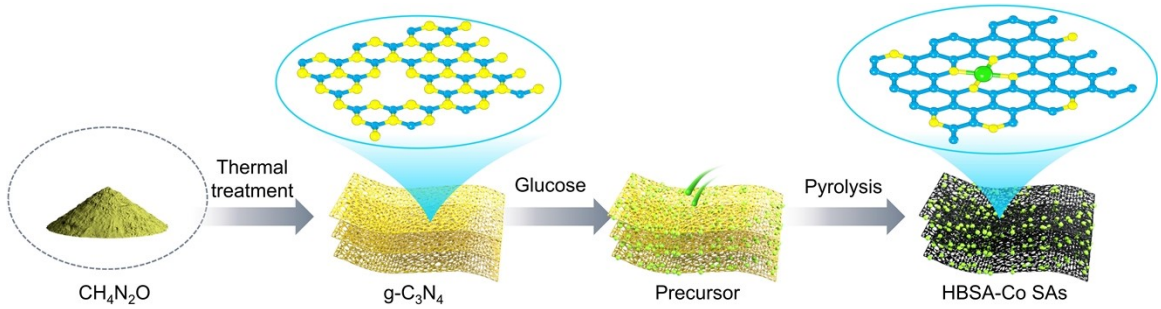

Figure S9. Schematic of the synthesis process for HBSA-Co SAs.

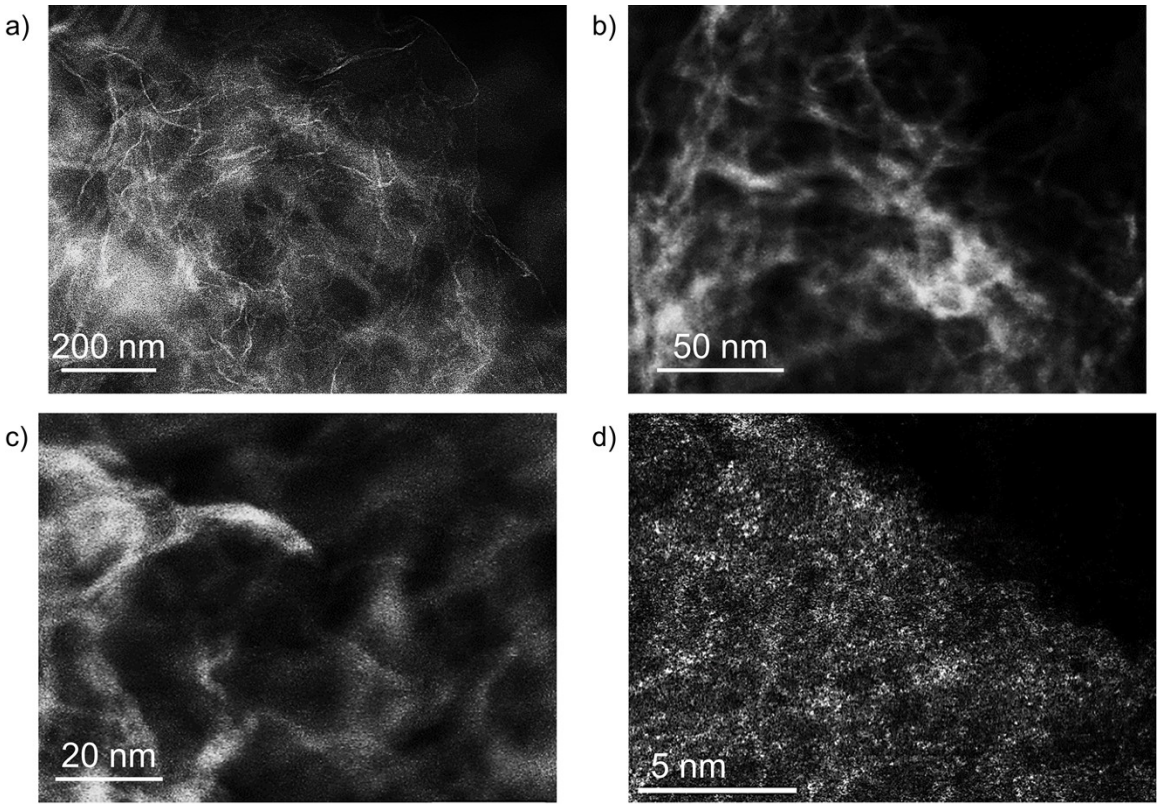

Figure S10. XRD patterns of (a) Co/NC, (b) Fe/NC, (c) Cr/NC, (d) NC.

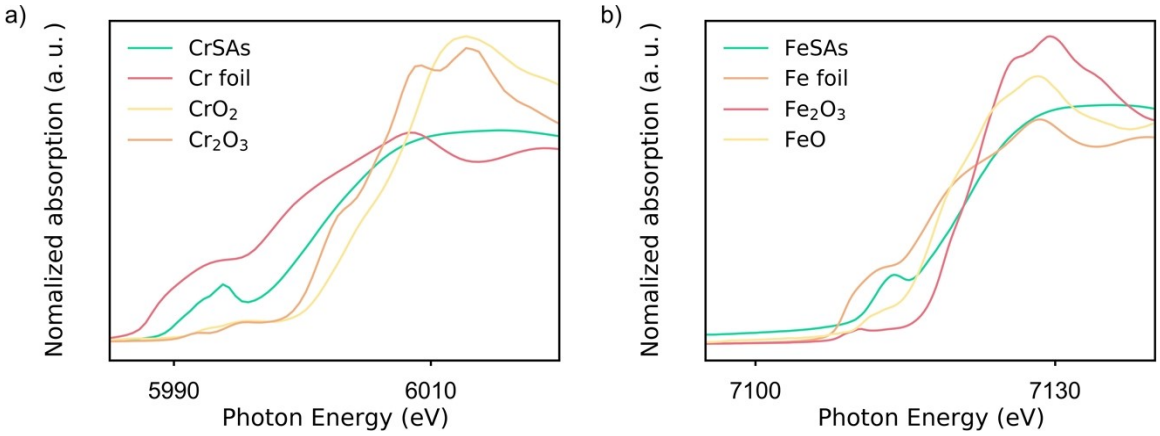

Figure S11. HAADF-STEM images of HBSA-Co SAs at different scales.

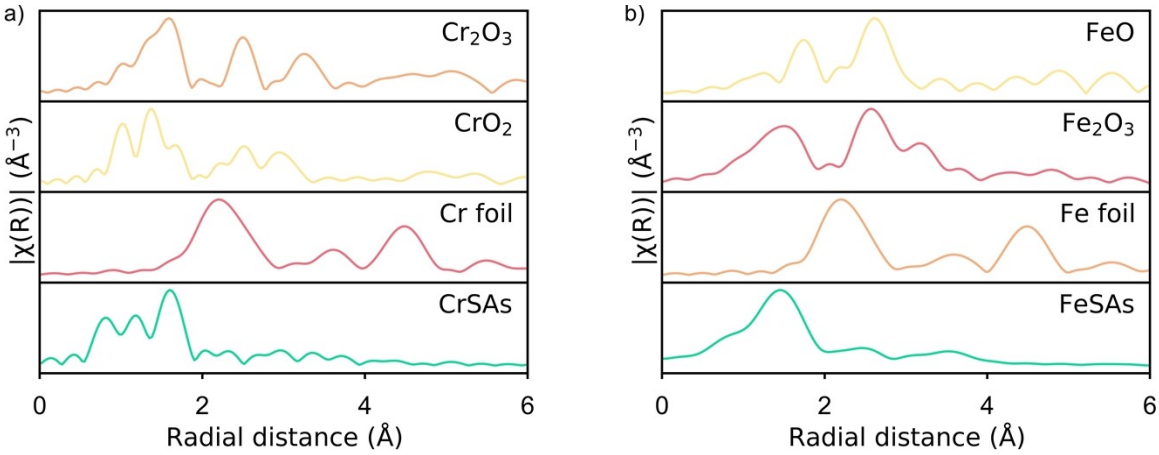

Figure S12. (a) Cr (b) Fe K-edge XANES spectra.

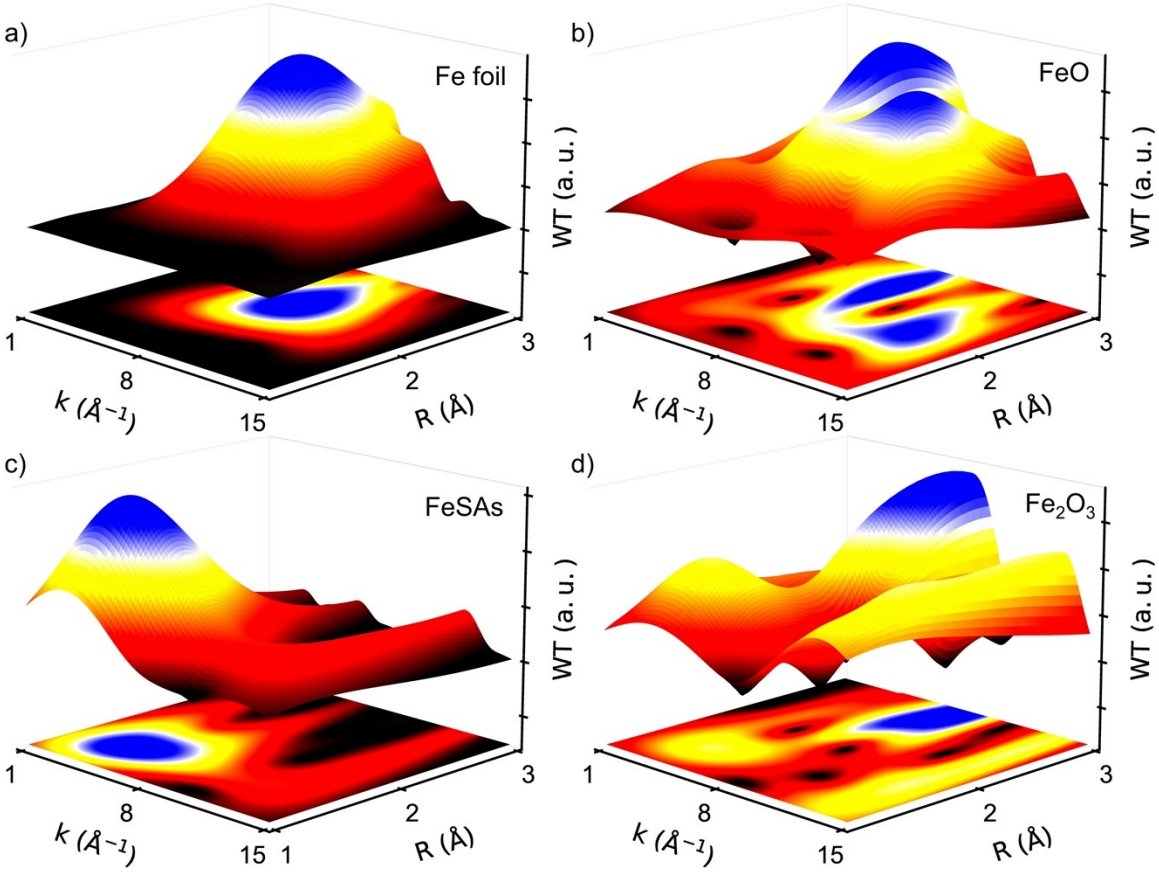

Figure S13. (a) Cr (b) Fe k3-weighted FT of EXAFS spectra.

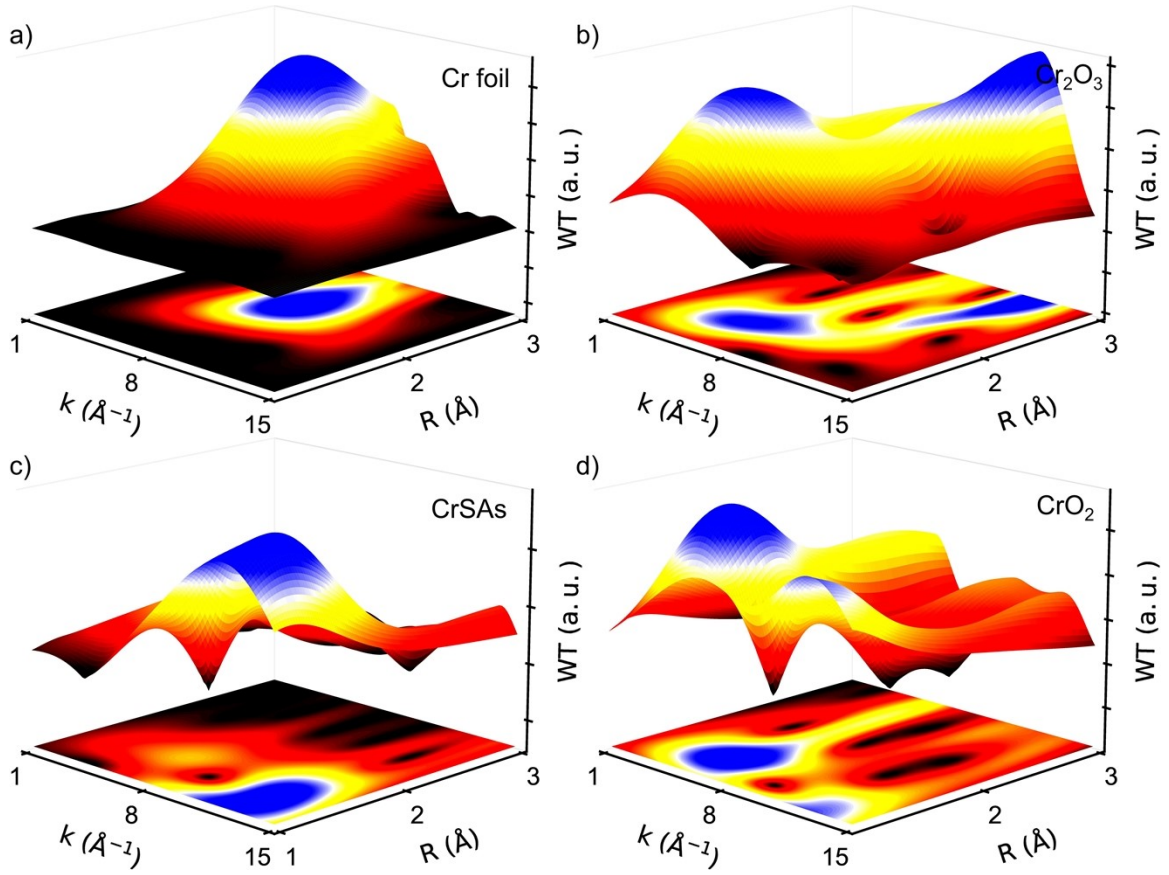

Figure S14. Fe K-edge WT-EXAFS spectra.

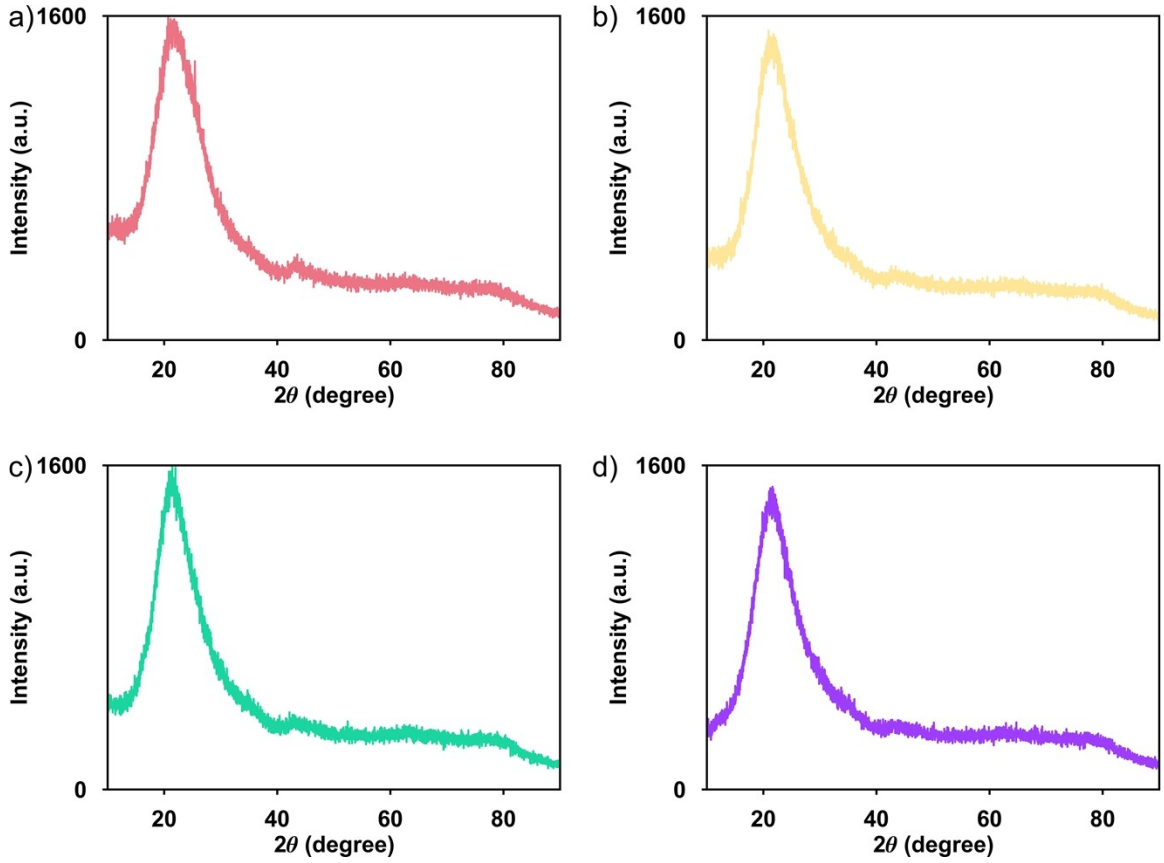

Figure S15. Cr K-edge WT-EXAFS spectra.

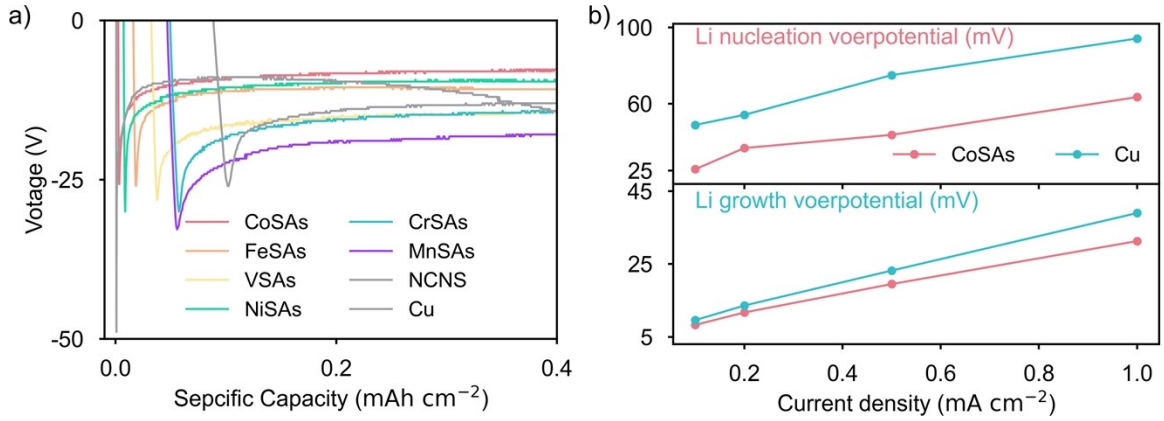

Figure S16. (a) First discharge curves on different matrices at $0.1\ mA\ cm^{-2}$; First discharge curves on (b) Relative nucleation overpotential (η_n) and growth overpotential (η_g) on HBSA-Co SAs and Cu foil at different current densities (0.1, 0.2, 0.5, 1.0 $mA\ cm^{-2}$).

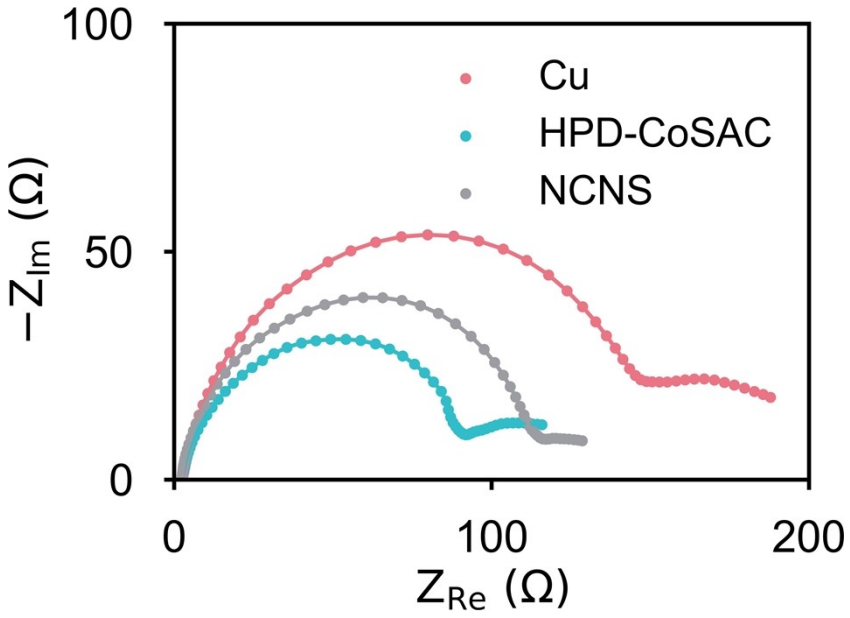

Figure S17. Nyquist plots taken on the HBSA-Co SAs, NC and Cu foil

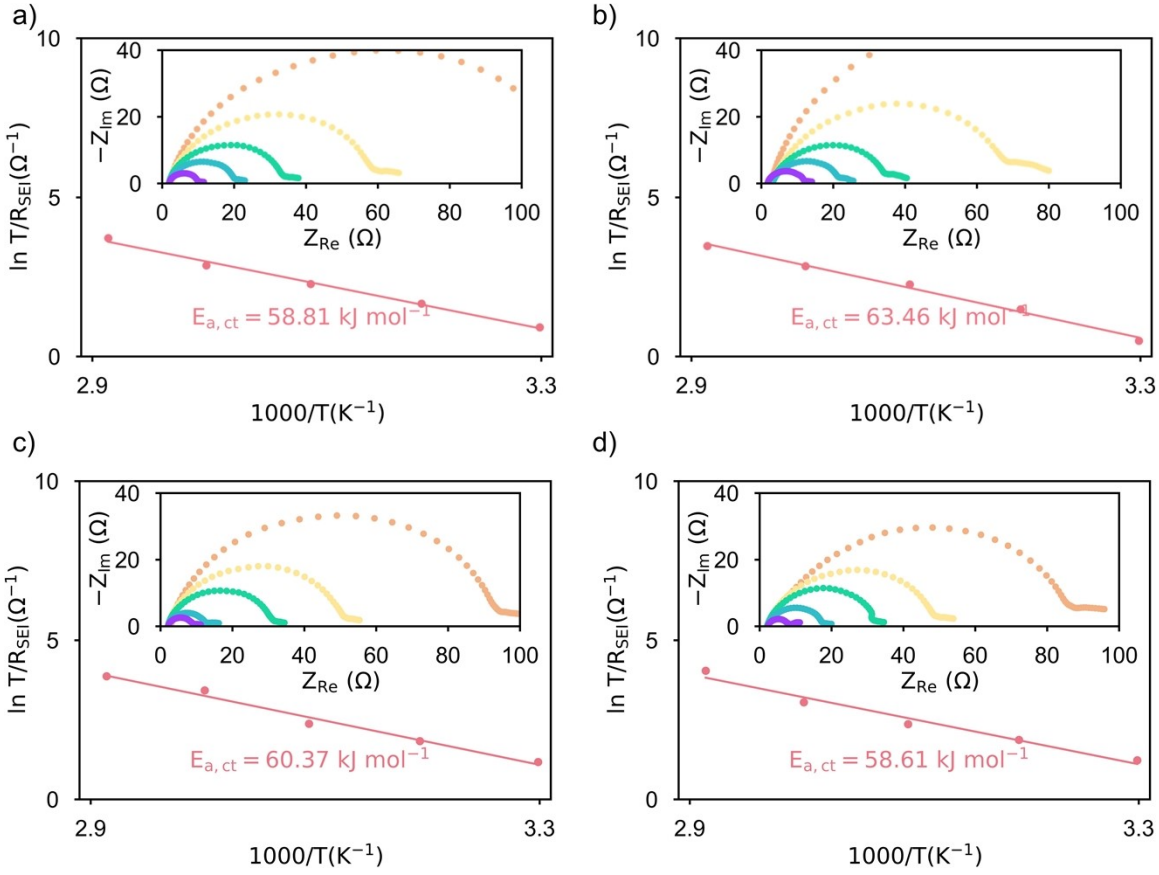

Figure S18. Temperature-dependent Nyquist plots taken on the (a) Li ⊂ NC, (b) Li ⊂ Cu foil, (c) Li ⊂ Fe-SAs and (d) Li ⊂ Cr-SAs.

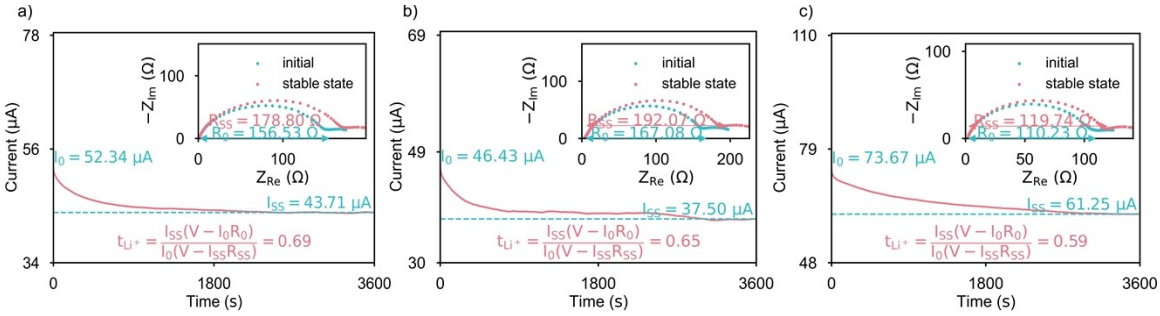

Figure S19. Chronoamperometric i-t and Nyquist plots taken on the (a) Li ⊂ HBSA-Co SAs (b) Li ⊂ NC (b) Li ⊂ Cu foil symmetrical cell.

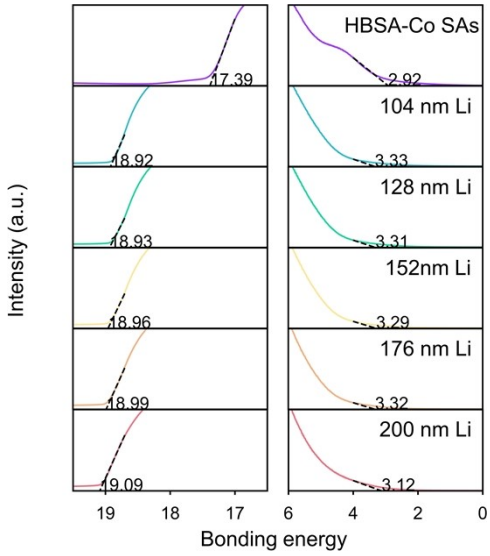

Figure S20. UPS spectra at states after etching for different times.

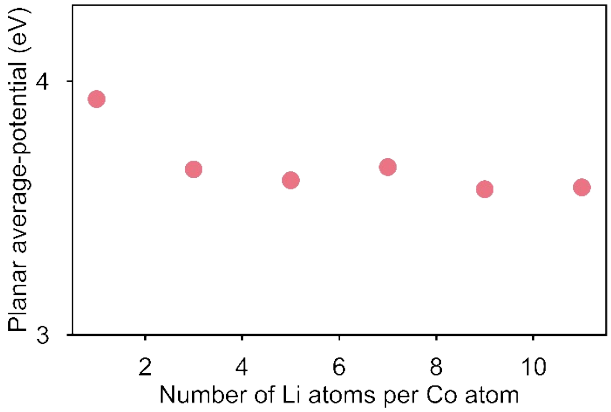

Figure S21. Surface work function (SWF) with different number of lithium atoms.

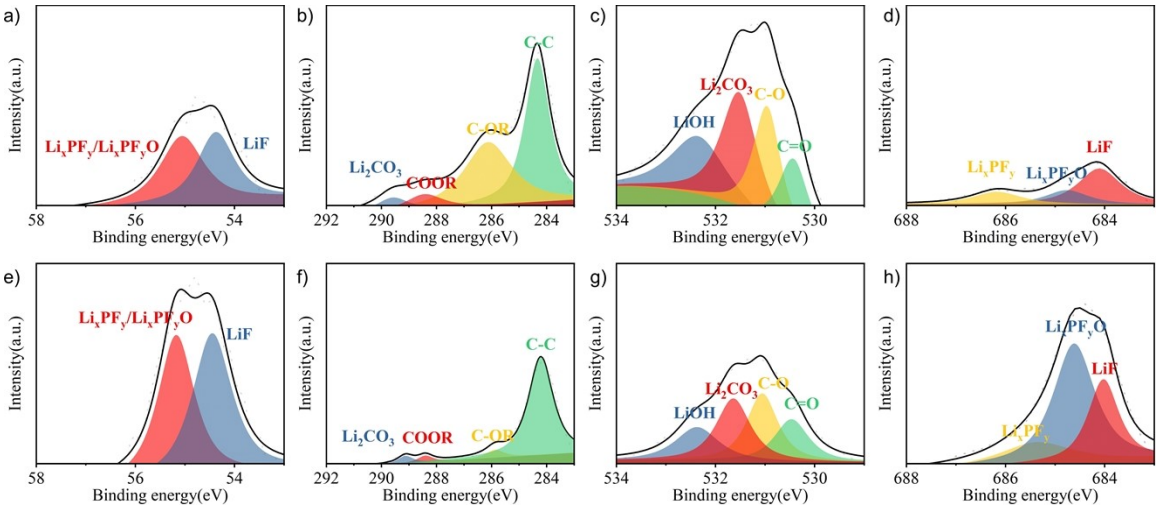

Figure S22. XPS spectra of lithium anode surface of (a~d) Cu current collector and (e~h) HBSA-Co SAs current collector after depositing $1\ mAh\ cm^{-2}$ of lithium metal.

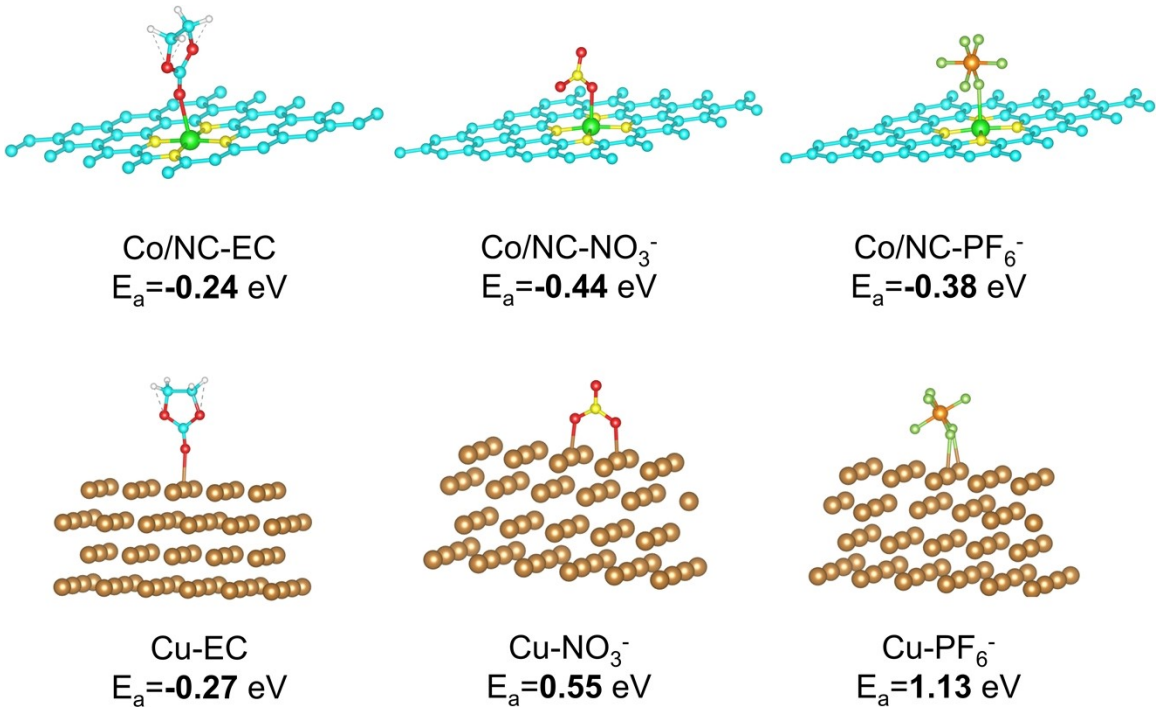

Figure S23. Adsorption energies of different molecules on Co single atoms and copper foil.

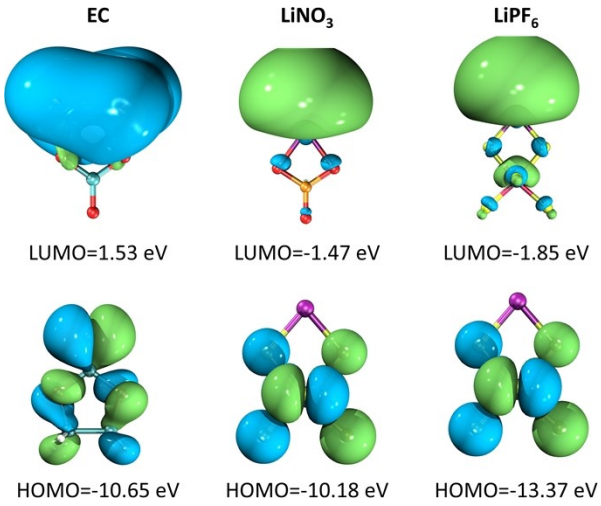

Figure S24. Calculation of HOMO and LUMO for different molecules.

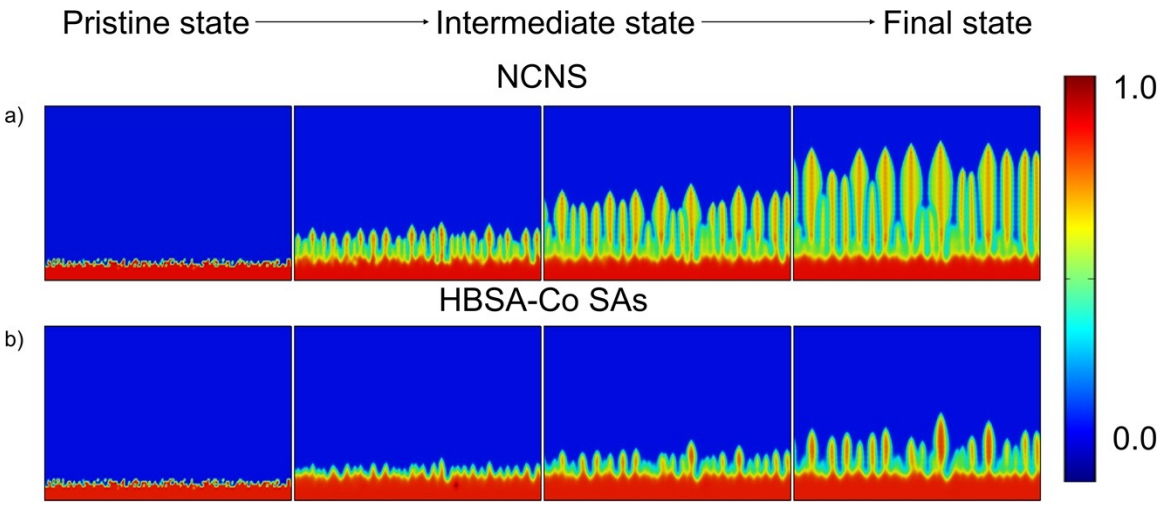

Figure S25. The evolution of line growth Li deposition morphology over time from phase field model.

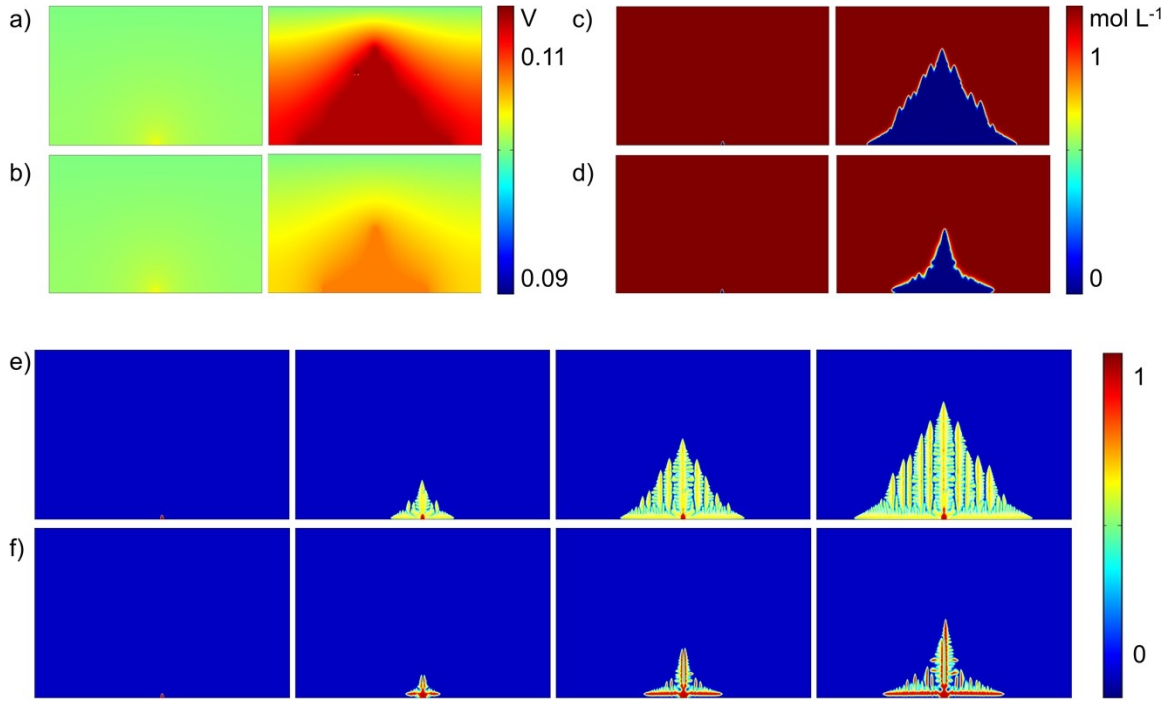

Figure S26. The evolution of point growth Li deposition morphology, internal electric field, and concentration field over time from phase field model.

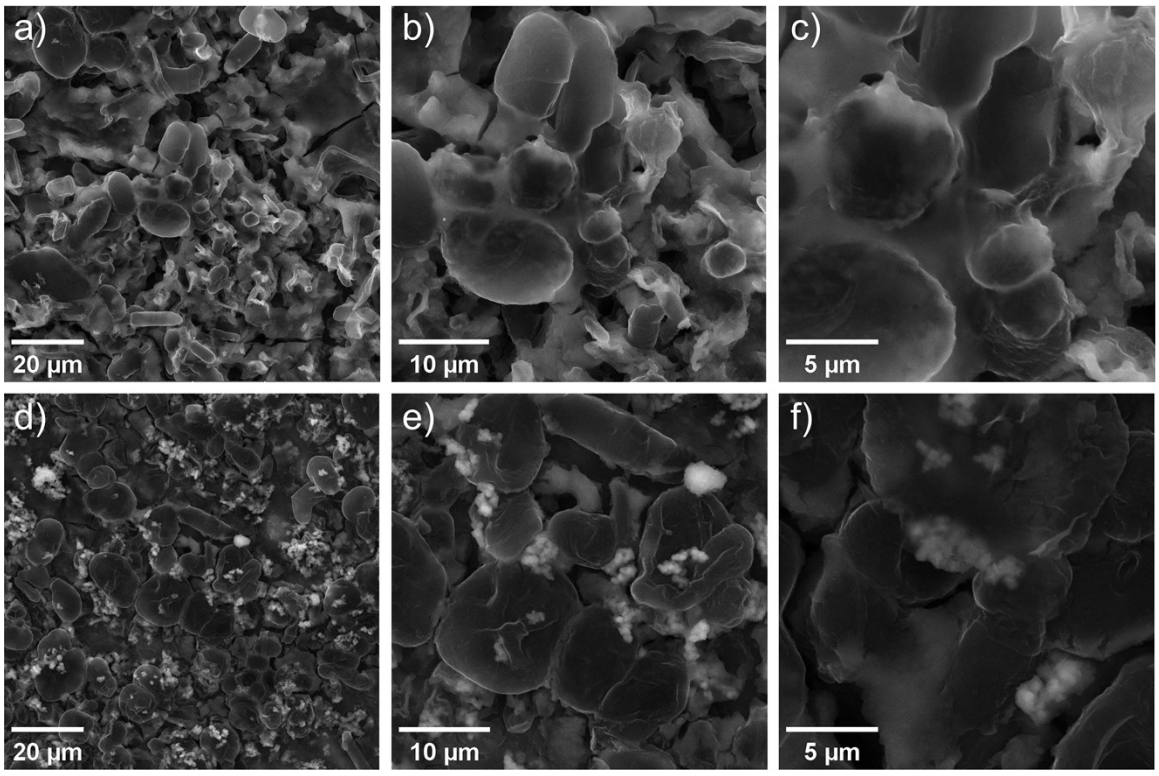

Figure S27. SEM images at different scales of (a~c) Cu current collector and (d~f) HBSA-Co SAs current collector after depositing $1\ mAh\ cm^{-2}$ of lithium metal.

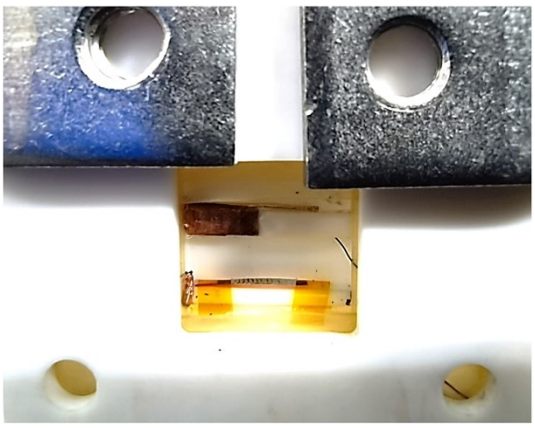

Figure S28. Photography of the in-situ optical dendrite testing mold.

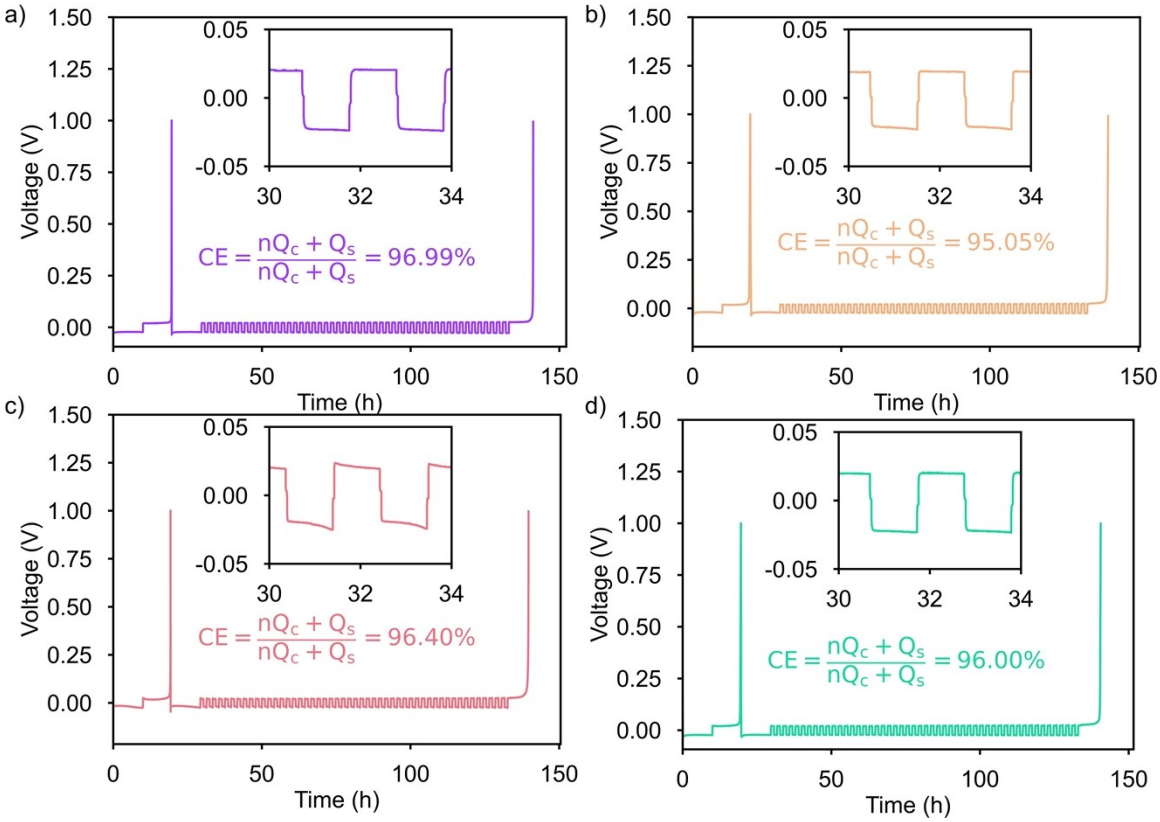

Figure S29. Coulombic efficiencies for (a) NC, (b) Cu foil, (c) Fe-SAs and (d) Cr-SAs in Aurbach CE test.

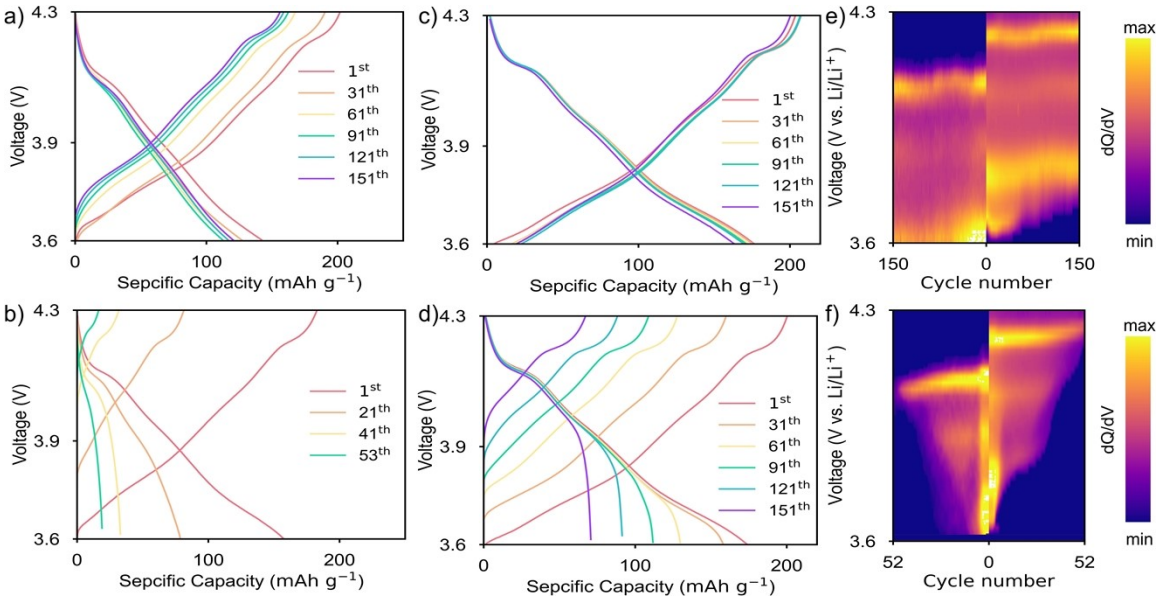

Figure S30. Charge-discharge curves for (a) NCM811||HBSA-Co SAs (b) NCM811||Cu (c) NCM811||$^{Li}\subset$HBSA-Co SAs and (d) NCM811||$^{Li}\subset$Cu full cells. Differential capacity heatmaps for (e) HBSA-Co SAs||NCM811 and (f) Cu||NCM811 full cells.

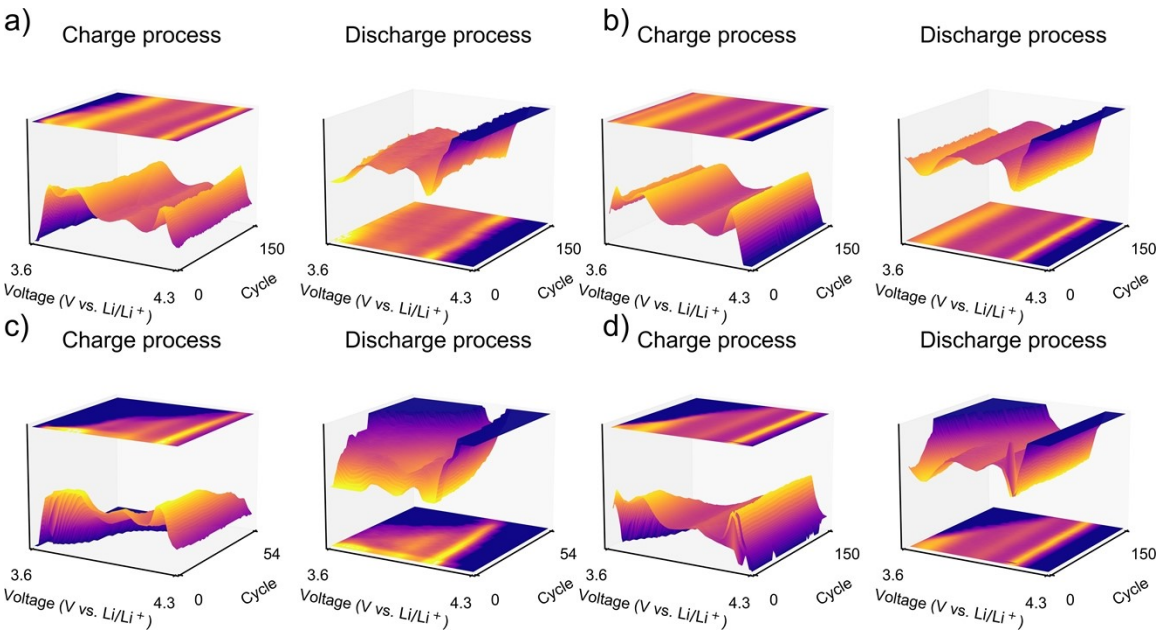

Figure S31. 3D differential capacity curve of (a) NCM811 ||HBSA-Co SAs (b) NCM811 ||Cu (c) NCM811||$^{Li}\subset$HBSA-Co SAs and (d) NCM811||$^{Li}\subset$Cu full cells.

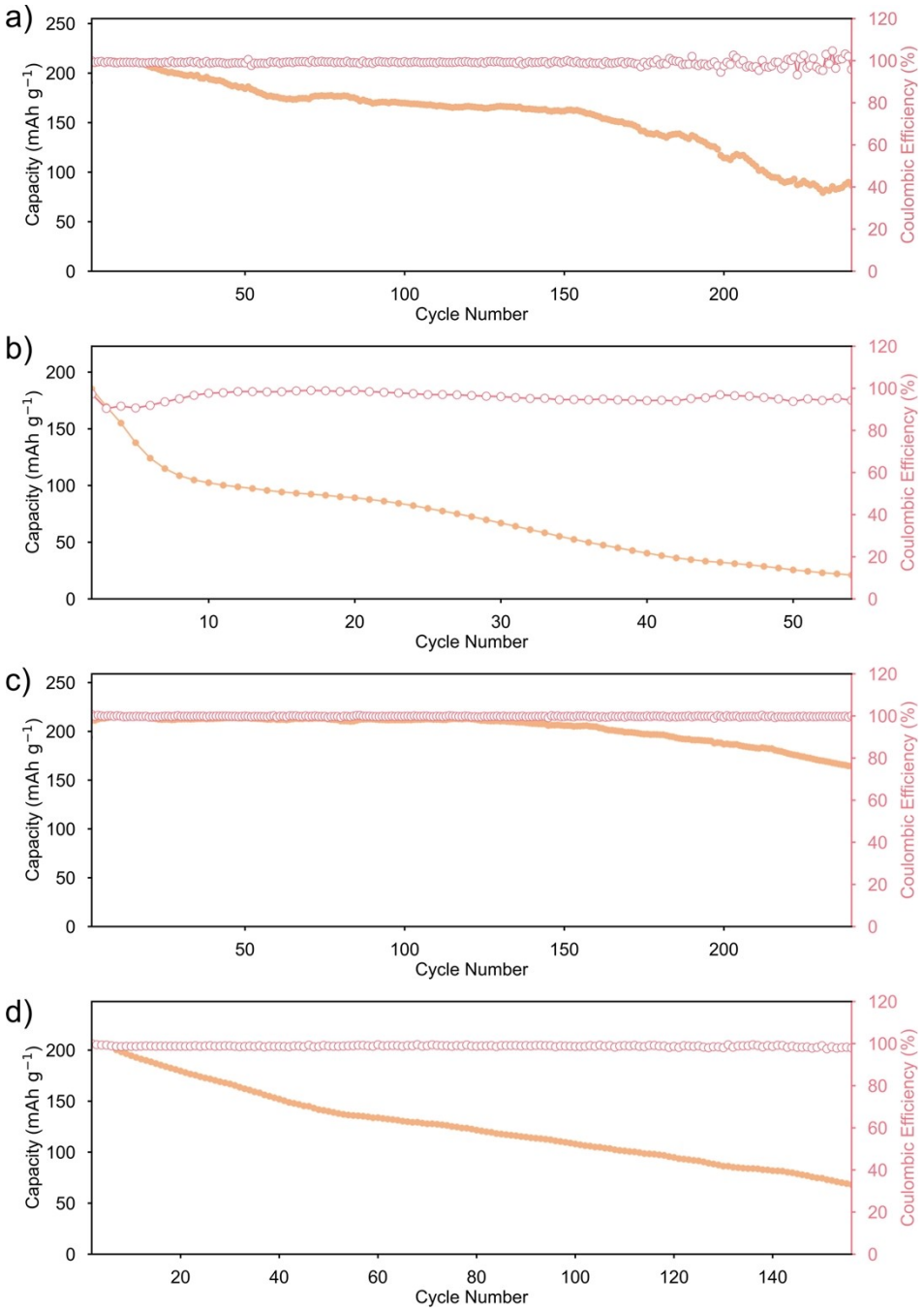

Figure S32. Cycling performance of (a) NCM811 ||HBSA-Co SAs (b) NCM811 ||Cu (c) NCM811 ||HBSA-Co SAs at N/P ratio of 1 (d) NCM811 ||Cu at N/P ratio of 1.

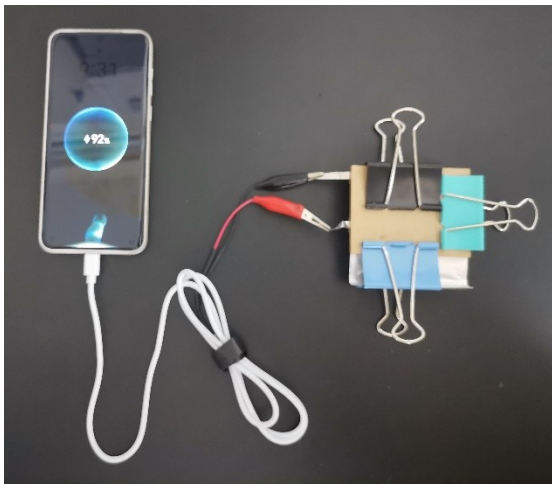

Figure S33. Charging a smartphone using an HBSA-Co SAs pouch cell.